▌ **Zeolitic Imidazolate Frameworks**

Vibrational Fingerprinting of Defects Sites in Thin Films of Zeolitic Imidazolate Frameworks

Bert M. Weckhuysen,* Zafer Öztürk, Rogier P. Brand, Jelle M. Boereboom, and Florian Meirer[a]

Abstract: Surface-mounted metal–organic frameworks (SUR-MOFs) are crystalline films of MOFs and have garnered a great deal of attention in the past years. So far, thin-film MOF research has been mainly focused on the synthesis and the exploration of potential applications of these materials, while a detailed understanding of their growth is still lacking. In this report evidence is provided for the inter-grown nature of surface-mounted thin films of Zn-ZIF-8 (SURZIF-8; ZIF = zeolitic imidazolate framework). Two distinct SURZIF-8 thin films have been made through layer-by-layer (LBL) growth after applying 20 and 50 LBL cycles. They have been characterized with atomic force microscopy (AFM) and Raman micro-spectroscopy. A detailed analysis of the Raman mapping data, inter alia using principal component analysis (PCA), revealed the existence of phase boundaries within the 20-cycle thin film, while the 50-cycle thin film is chemically more homogeneous. To further analyze these chemical heterogeneities, density functional theory (DFT) calculations were performed of three theoretical models providing spectroscopic fingerprints of the molecular vibrations associated with the Zn-ZIF-8 thin films. Based on these calculations and the experimental data distinct vibrational markers indicative for the presence of defects sites were identified.

Introduction

The recent decades have witnessed the discovery, characterization, and performance testing of a wide variety of metal–organic frameworks (MOFs) and related porous structures.[1–4] The fact that MOFs consist of both inorganic and organic building blocks provides ample opportunities to design MOFs with tunable functional properties, leading to various applications in the fields of catalysis,[5–7] drug delivery,[8,9] sensing,[10,11] biomedical imaging,[8] and gas adsorption.[12–14] An emerging class of MOFs are zeolitic imidazolate frameworks (ZIFs).[15] The word "zeolitic" is derived from their zeolite-like framework topologies, while the term "imidazolate" relates to the presence of imidazolate linkers or their derivatives. ZIFs are formed through tetrahedral coordination of transition-metal ions (e.g., Co^{2+}, Zn^{2+}, Cu^{2+} or Fe^{2+}) with imidazolates or its derivatives acting in the same way as silicon and aluminum atoms when covalently joined by the bridging of oxygen atoms in zeolites.[16,17] Since the metal-ion/imidazolate/metal-ion angle is similar to the 145° Si^{4+}-O-Si^{4+} angle in zeolites, ZIFs have zeolite-like topologies. One of the prototype materials of the ZIF family is Zn-ZIF-8, one of the most widely studied ZIFs.[18–21] Zn-ZIF-8 is composed of Zn^{2+} ions tetrahedrally coordinated to bridging 2-methylimidazolates, and has the sodalite topology with 1.16 nm wide cavities formed by 4-ring and 6-ring Zn-N_4 clusters leading to 0.34 nm wide windows.[20–24]

There has been substantial attention towards the growing of MOFs in the form of a thin layer anchored to a surface, which are known as surface-mounted metal–organic frameworks (SURMOFs).[15,25–27] The thin-film morphology of MOFs is required in certain applications for their proper functioning, which is unfortunately not available for MOF powders with a few µm of particle size.[25] MOF thin films have potential use in the fields of luminescence,[28] quartz crystal microbalance-based sensors,[29,30] catalysis,[31,32] as well as gas separation.[33–35] So far three main strategies have been reported in literature for the preparation of SURMOFs: 1) direct growth from a mother liquor, 2) assembly of preformed MOF crystals, and 3) the step-wise layer-by-layer (LBL) growth onto a substrate.[26,27] For LBL growth of SURMOFs, functionalized substrates are vital for directing the nucleation, orientation, and the structure of the MOF growth.[36] Similarly, ZIF thin films can be prepared by direct synthesis, seeded growth, electrochemical methods, and assembly of preformed crystals.[25,26]

Herein we present the synthesis of thin films of ZIF-8 (SURZIF-8) by using the stepwise LBL method. Two distinct SURZIF-8 samples were prepared by applying 20 and 50 LBL

[a] Prof. Dr. B. M. Weckhuysen, Z. Öztürk, R. P. Brand, J. M. Boereboom, Dr. F. Meirer
Inorganic Chemistry and Catalysis
Debye Institute for Nanomaterials Science, Utrecht University
Universiteitsweg 99, 3584 CG Utrecht (The Netherlands)
E-mail: b.m.weckhuysen@uu.nl

cycles. A detailed chemical imaging of these two materials was provided by Raman micro-spectroscopy, while for the height information and the surface morphology atomic force microscopy (AFM) was used. The AFM maps revealed morphological differences between the 20-cycle and 50-cycle thin films, and for the 20-cycle sample it was furthermore possible to correlate these morphological features with distinct spectral features in the Raman data. In order to further investigate the spatial variation of spectroscopic features within each sample in an unbiased way principal component analysis (PCA) and subsequent clustering were performed. The resulting maps showed regions with distinct spectral characteristics that were found more heterogeneously distributed in the 20-cycle sample than in the 50-cycle sample.

To link these distinct spectral features and their variation to structural information density functional theory (DFT) calculations for model clusters were conducted, helping to identify the observed experimental vibrations and their spatial variation. DFT allowed for the identification of fingerprint vibrations, providing insight in the structural heterogeneities present within the two Zn-ZIF-8 thin films under study. This detailed analysis of the Raman spectral maps revealed the presence of defects sites and allowed for the identification of diagnostic Raman bands, which undergo intensity changes and/or band splitting/shifts, indicative for structural defects in the material.

Results and Discussion

Combined AFM–Raman mapping of SURZIF-8 thin films

AFM measurements were performed in a region of $100 \times 100 \ \mu m^2$ in order to obtain spatially resolved information on the morphology and height of the two thin-film samples under study. Figure 1 shows the AFM scans obtained for the Zn-ZIF-8 thin films recorded after 20 and 50 LBL cycles. Note that the defect observed as a blue area in the center of the AFM micrograph of the 20-cycle Zn-ZIF-8 thin-film material originates from a too long Raman laser exposure during the Raman micro-spectroscopy measurements executed before performing the AFM scans. This illustrates that the Zn-ZIF-8 thin films prepared are rather sensitive to laser irradiation, but also provides a means to make a spectroscopic marker for internal calibration of the AFM and Raman data.

The maximum height difference within each AFM map was found to be higher in the 50-cycle Zn-ZIF-8 sample than in the 20-cycle Zn-ZIF-8 sample ($\approx 3 \ \mu m$ versus $\approx 1.7 \ \mu m$ when considering the hole). The reason for this larger height difference is that the 50-cycle Zn-ZIF-8 thin-film sample contains two large grains, clearly visible in Figure 1b. Furthermore, the number of grains seems higher in the case of the 20-cycle Zn-ZIF-8 sample indicating that after 30 additional cycles a more homogeneous and more inter-connected thin film is formed due to a decreasing distance between the individual Zn-ZIF-8 grains formed. The number of grains in both sample regions
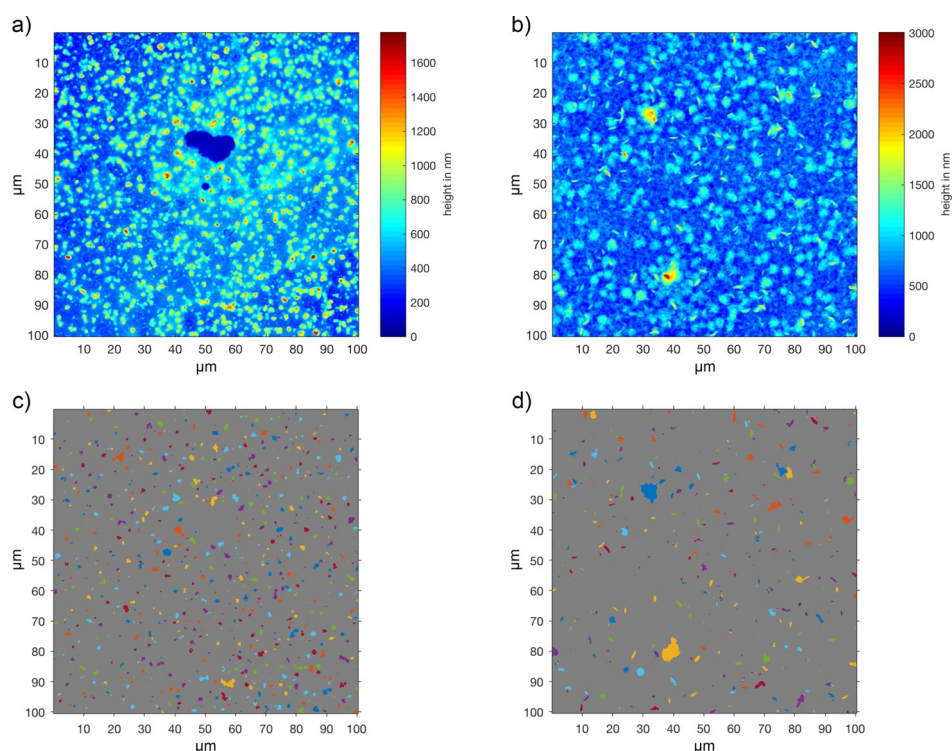

Figure 1. Atomic force microscopy (AFM) micrographs of two Zn-ZIF-8 thin films as made by the layer-by-layer (LBL) synthesis method: a) 20-cycle Zn-ZIF-8 thin film and b) 50-cycle Zn-ZIF-8 thin film. Panels c) and d) display the result of the grain analysis performed with each AFM map. Each individually colored region in these images represents and isolated grain, while the background is indicated in gray. The maps indicate morphological differences in grain sizes and shapes.
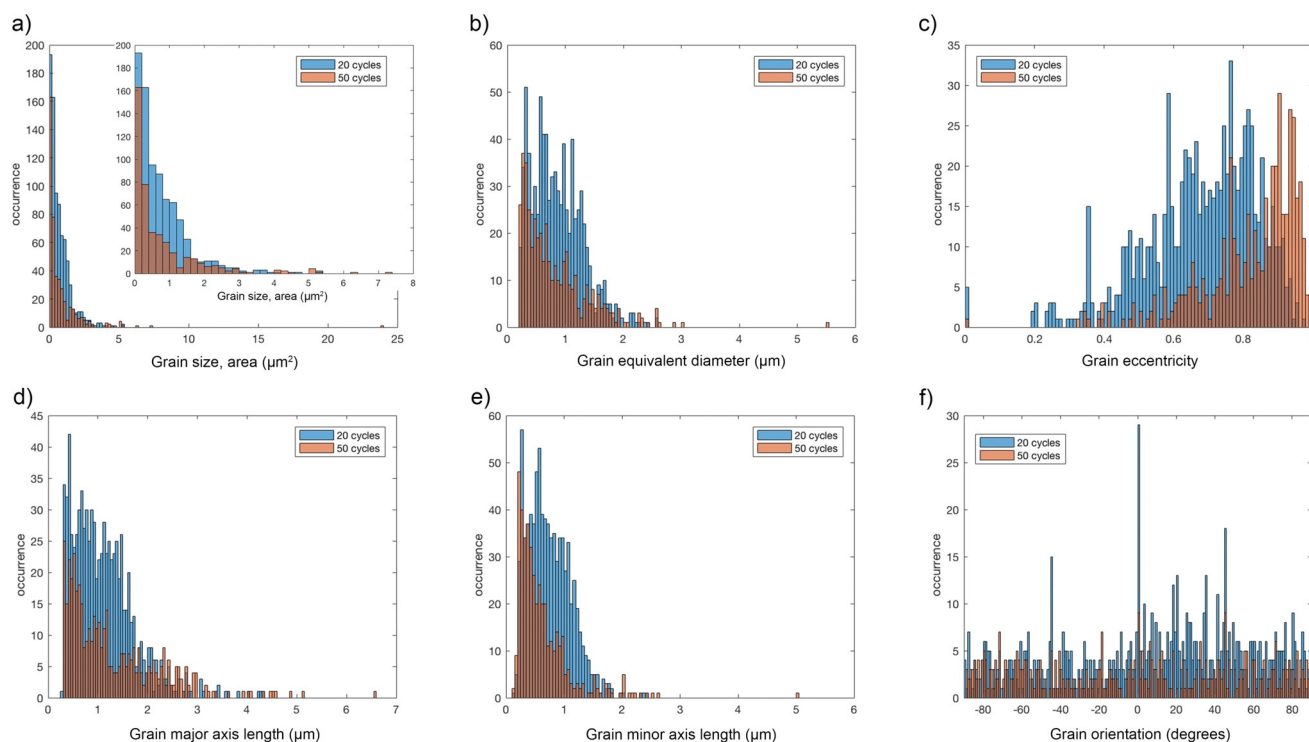
Figure 2. Grain analysis based on the atomic force microscopy (AFM) micrographs of two Zn-ZIF-8 thin films as made by the layer-by-layer (LBL) synthesis method: the blue bars indicate the 20-cycle Zn-ZIF-8 thin film, while the red bars denote the 50-cycle Zn-ZIF-8 thin film. Panels a) through f) report the results of the grain analysis: a) grain size distribution, b) grain equivalent diameter, c) grain eccentricity (a value between 0 and 1, where 0 indicates a circle), d) and e) the major and minor axis length of an ellipse that has the same second-moments as the grain, respectively, and f) the grain orientation expressed as the angle in degrees between x-axis and the major axis of this ellipse.

was computed based on the AFM image segmentation described in the experimental section and determined as 819 and 438 grains for the 20-cycle and 50-cycle material, respectively. The region properties of each grain, namely region area, eccentricity, major and minor axis length, and orientation are reported in Figure 2. The grain size distributions confirm what can be seen in the AFM maps: most grains are smaller than 2 µm, while the 50-cycle sample show fewer grains in the region around 1 µm, but several very large grains. Stronger morphological differences are observed when inspecting parameters that describe the shape of the grains. Here many grains in the 50-cycle sample show a needle- or platelet-like morphology, which is reflected by a grain eccentricity distribution that is clearly shifted towards values closer to 1, that is, less circular shapes, and the fact that very few grains show a minor axis length larger than 1 µm, while a significant population has major axis lengths larger than 1 µm. However, as can be seen in Figure 2 f, neither the more spherical grains in the 20-cycle sample nor the more elongated grains in the 50-cycle sample showed a significantly preferred orientation. The larger number of grains with an orientation of 0° for the 20-cycle sample does not indicate a preferred orientation, but is a result of a larger number of almost perfectly spherical grains for which no orientation can be computed.

In addition to the morphological information acquired from the AFM data, we performed Raman micro-spectroscopy measurements on both samples in order to provide chemical infor-

mation regarding the formation of Zn-ZIF-8 thin-film material. In addition to micro-spectroscopic Raman maps we have recorded bulk Raman spectra for both samples. These spectra are displayed in Figure 3 a and 3 b for the 20-cycle and 50-cycle Zn-ZIF-8 thin films, respectively. These Raman spectra of the thin films confirm that the chemical bond structure corresponds to the one previously reported in the literature for Zn-ZIF-8.[13,37] The Raman spectra of Zn-ZIF-8 exhibited characteristic bands, namely, Zn—N stretching (≈ 139 cm^{-1}; strong) imidazole ring puckering (≈ 686 cm^{-1}; very strong), C=C stretching (≈ 1505 cm^{-1}; strong), CH$_3$ (≈ 2926 cm^{-1}; moderate), and C—H aromatic (≈ 3130 cm^{-1}; very weak) stretching modes.[13,38] A comparison of these bulk Raman spectra of the 20-cycle and 50-cycle thin films clearly reveal spectral differences arising from 1) intensity changes and 2) band aspect ratio variations along with band broadening/splitting and also spectral shifts. These spectral differences and variations require further analysis as they may provide a scientific basis to determine a set of spectroscopic fingerprints for defect sites in SURZIF-8 thin films, and MOF and ZIF materials in general. This is the topic of this research work.

To accomplish this goal, we have performed combined AFM and Raman mapping measurements as one may expect that the topology differences in the AFM maps for both samples may harbor these important spectral changes. Raman micro-spectroscopy maps have therefore been recorded for the same 100×100 µm^2 region of each of the two Zn-ZIF-8 thin films, as
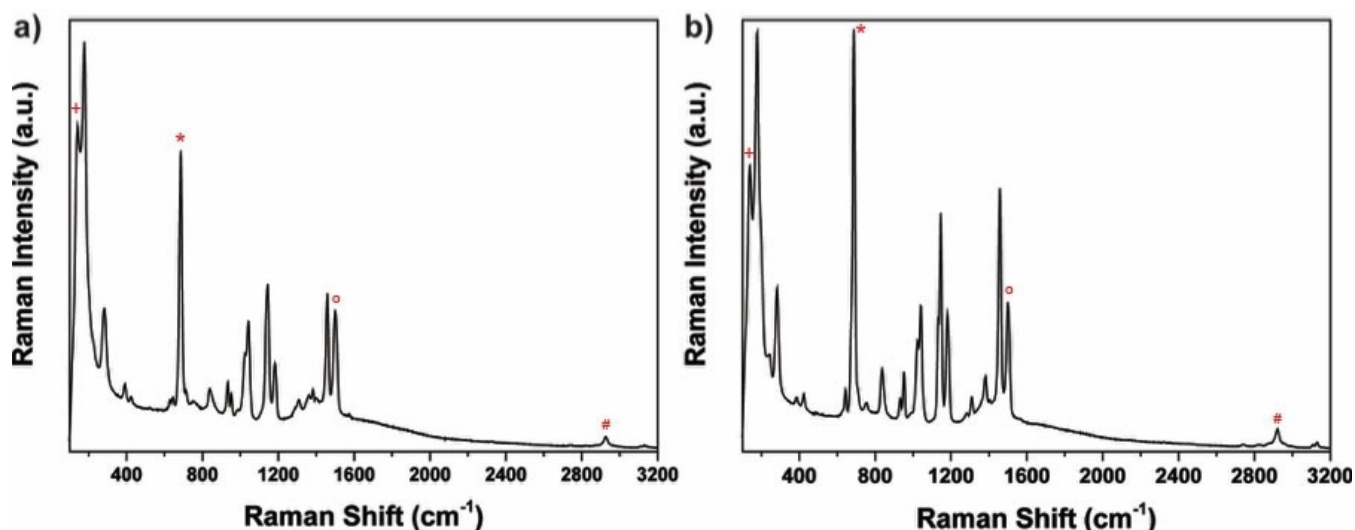
Figure 3. Characteristic Raman spectra of two Zn-ZIF-8 thin films as made by the layer-by-layer (LBL) synthesis method: a) 20-cycle Zn-ZIF-8 thin film b) and 50-cycle Zn-ZIF-8 thin film. Markers indicate the characteristic bands for Zn-ZIF-8: (+) Zn-N stretching (≈ 139 cm^{-1}), (*) imidazole ring puckering (≈ 686 cm^{-1}), (o) C=C stretching (≈ 1505 cm^{-1}), and (#) CH3 (≈ 2926 cm^{-1}) stretching modes.[13,40] A very weak C–H aromatic (≈ 3130 cm^{-1}) stretching vibration can also be noticed.

displayed in Figure 1, with the aim to correlate topographical and spectroscopic information. Raman micro-spectroscopic mapping was carried out for two sub-spectral regions, namely 1) a set of Raman spectra, which center at 520 cm^{-1} and 2) a

set of Raman spectra, which center at 1180 cm^{-1}, thereby covering the two spectral regions from 100 to 950 cm^{-1} and from 800 to 1550 cm^{-1}, respectively . All measured Raman spectra were pre-processed, by subtracting the background and nor-
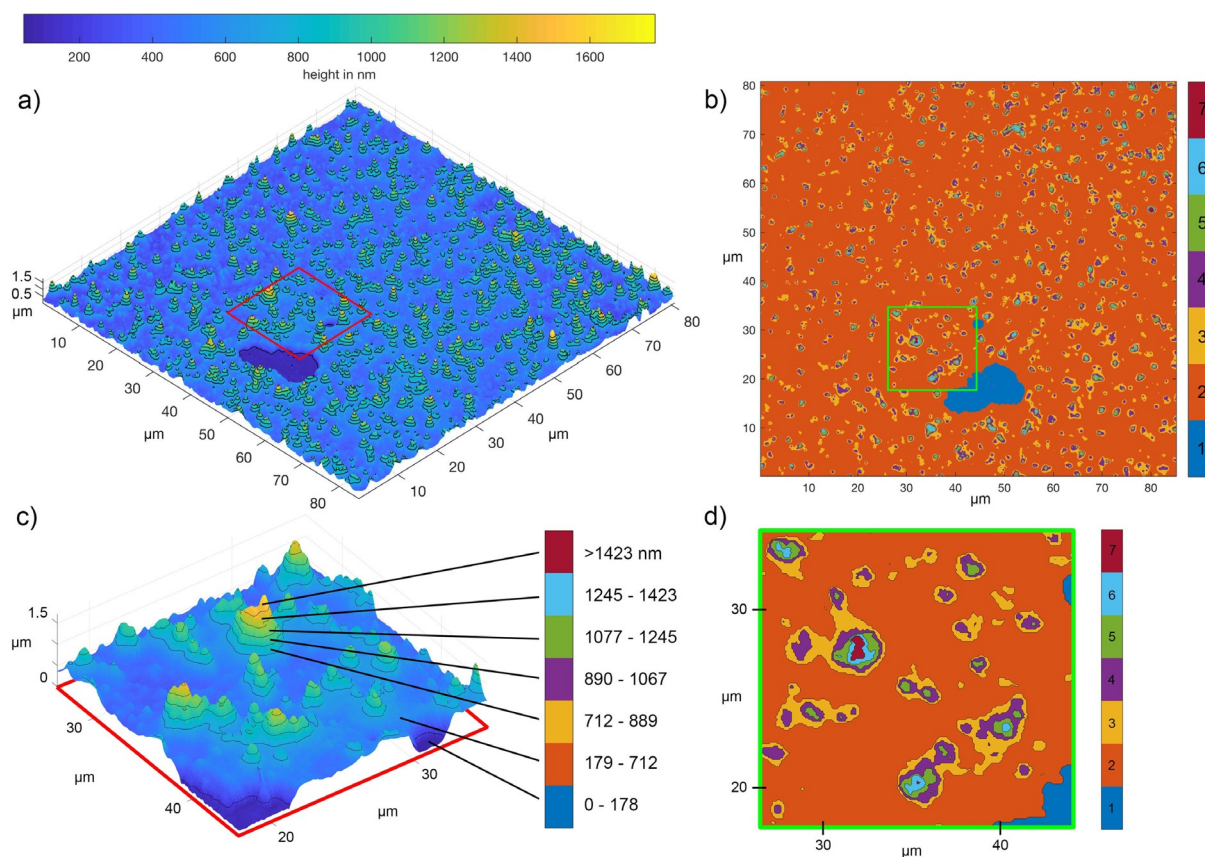

Figure 4. Height-based segmentation of the atomic force microscopy (AFM) data recorded for the 20-cycle Zn-ZIF-8 thin-film data. The 7 obtained regions displayed in panels b) and d) were then used to obtain the average Raman spectrum of each region from the Raman maps recorded for the same sample area. Panels c) and d) show a zoom of the regions indicated by the red and green square in the maps displayed in panels a) and b), respectively.

malizing every individual spectrum to its own minimum and maximum values.

For the 20-cycle sample it was possible to align AFM and Raman maps by image registration using the above-mentioned hole in the sample as a fiducial maker (blue area, Figure 1). The result of this data registration is displayed in Figure 4. In order to investigate a possible correlation between topographical and spectroscopic features the height information from the AFM data was used to segment the mapped sample area into seven regions, each covering a specific height range. The resulting map in which each of these regions is indicated by a specific color is displayed in Figure 4b. Next, the average Raman spectrum of each region was determined by masking the Raman spectral maps based on this segmentation, that is, computing the average spectrum of all the Raman spectra located in each region. The result of this analysis is reported in Figure 5 showing the average spectra of all seven regions for both investigated spectral regions. In these plots it is clearly visible that the highest regions of the thin film formed by the 20-cycle Zn-ZIF-8 show differences in its spectral features.

Motivated by these initial findings PCA and subsequent clustering were then used to further study variations in both sets of Raman spectra and for both samples. Details of this approach can be found in the Experimental Section. This ap-

proach effectively segmented the data into regions of strongest spectral similarity. Here it is important to note that this segmentation method is 1) unbiased, as it requires no human input other than the number of clusters, and 2) purely based on spectral similarity and not on any other correlation such as spatial proximity or sample height. We also want to point out that although we use the term "phase" in the following discussion, PCA and clustering methods do not segment spectroscopic data into pure chemical phases (or Raman spectra thereof) but into the predetermined number of groups of most similar Raman spectra, which in almost all cases still contain mixtures of "pure" phases. The results of this analysis are displayed in Figures 6 and 7 for the two spectral regions centered at 520 cm^{-1} and 1180 cm^{-1}, respectively.

For the first spectral region of interest (100–950 cm^{-1}), the results for both the 20-cycle and 50-cycle thin-film samples are provided in Figure 6a and 6b, respectively. Pixels with the same color within an individual image correspond to the same cluster indicating mutual spectral similarity, which can be evaluated from the averaged cluster Raman spectra, given in Figure 6c and 6d. The same color codes were used for these spectra in line with their clustering analogues for clarity.

Very interestingly, Figure 6a shows a clear phase boundary in the cluster maps of the 20-cycle thin-film sample between
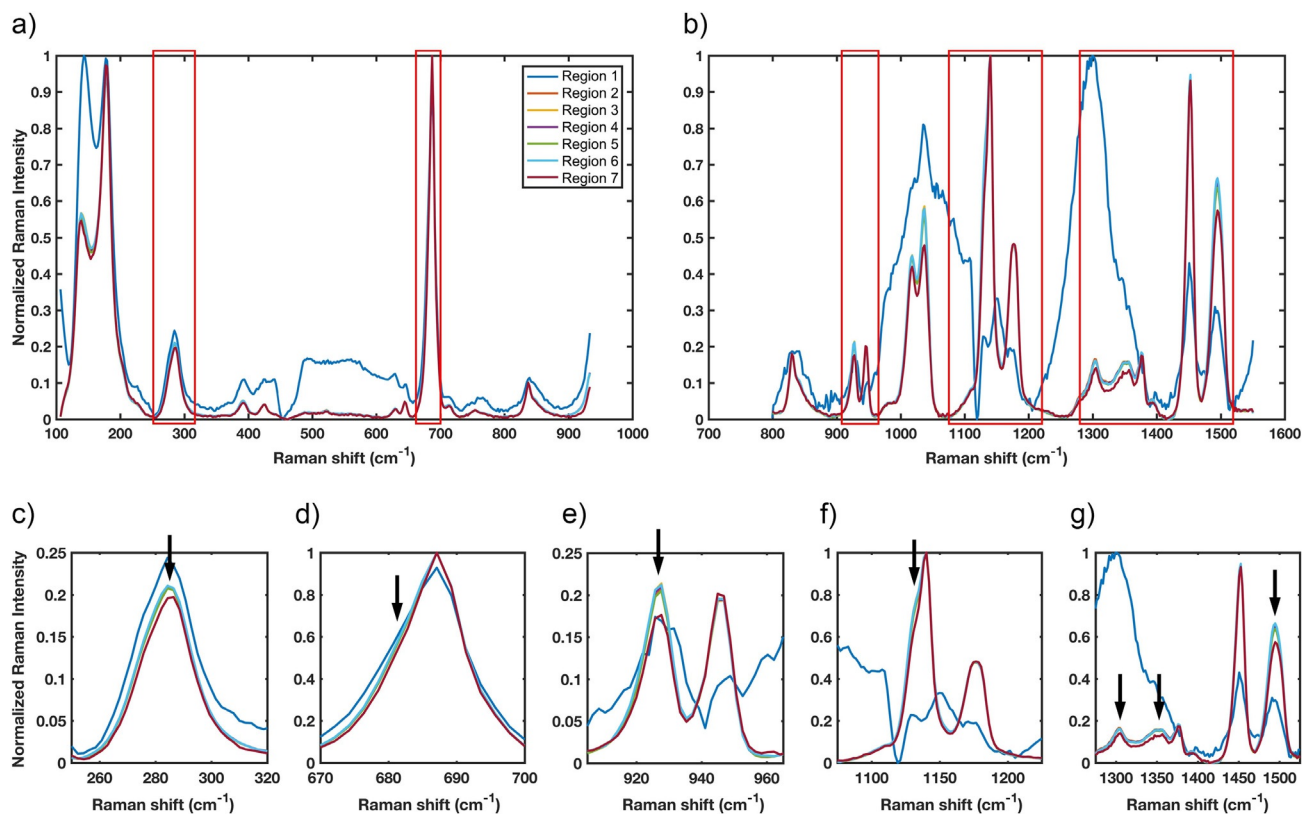

Figure 5. Average Raman spectra of the 7 regions obtained from the height-based image segmentation of the atomic force microscopy (AFM) data recorded for the 20-cycle Zn-ZIF-8 thin film (see Figure 4). Region 1 indicates the Raman signal obtained in the region where the thin film has a hole. Regions 2 to 7 indicated areas of increasing height of the thin film. Panels a) and b) display the two spectral regions recorded during Raman mapping (the region reported in panel a) centers at 520 cm^{-1} and the region shown in panel b) centers at 1180 cm^{-1}). Panels c) to g) display close-ups of the spectral bands indicated by the red frames in panels a) and b), that is, regions where the strongest changes in the features of the Raman spectra are visible. It becomes clear that the highest regions of the thin film display differences in these spectral bands when compared to the other areas of the sample–these differences are indicated by black arrows in panels c) to g).
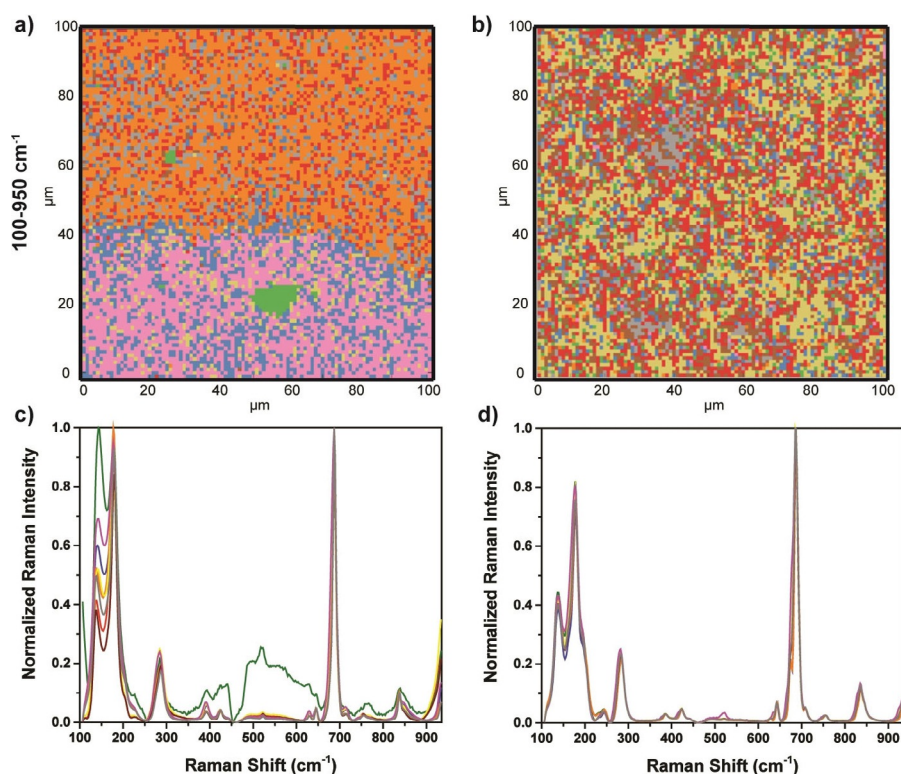
Figure 6. Result of principal component analysis (PCA) and subsequent clustering of the Raman microscopy maps for the 100–950 cm^{-1} spectral region for a) the 20-cycle Zn-ZIF-8 thin film and b) the 50-cycle Zn-ZIF-8 thin film. The average Raman spectra belonging to the different clusters obtained from PCA and clustering are displayed in panels c) and d) both for the 20-cycle Zn-ZIF-8 thin film and the 50-cycle Zn-ZIF-8 thin film, respectively. Corresponding colors indicate, which spectrum belongs to which cluster.

the upper and lower half of the Raman map in the 100–900 cm^{-1} spectral region. Figure 6c gives insights into the differences observed in the Raman maps of the 20-cycle thin-film sample as the comparison of the spectra of the clusters shows intensity and band ratio differences as well as band broadening and spectral shifts. In Figure 6a, the Raman spectra of the clusters colored red, orange, brown and grey share similar spectral features (mainly located in the upper part of the Raman map), whereas the other three clusters, namely blue, yellow and magenta (mainly located in the lower part of the Raman map) share a lot of spectral similarities. The spectral differences between these two groups are the origin of the observed phase boundary. Note that the orange and magenta clusters dominate the upper and lower half of the Raman map, respectively. Furthermore, the blue cluster is found in both the upper and lower region of the map recorded for the 20-cycle thin-film sample, but predominantly in the lower region and at the phase boundary and seems to act as an intermediate between the two observed main phases. The green cluster is perfectly correlated with the hole in the sample and indicates a group of spectra that are heavily distorted and have therefore been pooled together by PCA and clustering.

It is important to stress here that the observed phase boundary is completely absent in the corresponding AFM micrograph of the 20-cycle thin-film sample (Figures 1a and 4a), because AFM is not able to detect chemical heterogeneities and the observed chemical differences are not correlated to topo-

graphical features. In other words, the observed observations in height and grain size are not sufficient to explain the chemical differences observed in the Raman spectra. From the Raman spectra, shown in Figure 6c, it is clear that spectra in the lower part are clearly distinct from those found in the Raman map of the 50-cycle thin-film sample, which is shown in Figure 6b. This Raman map reveals a more homogeneous nature of the Zn-ZIF-8 thin-film sample. All clusters are indeed more or less homogenously distributed throughout the Raman map, while the Raman spectra corresponding to each of the clusters (Figure 6d) are very similar, evidencing that there is not much spectral variance in the Raman data measured for this sample.

For the second spectral region of interest (800–1550 cm^{-1}), the results of PCA and clustering of the data recorded for both the 20-cycle and 50-cycle thin-film samples are provided in Figures 7a and 7b, respectively. Again, pixels with the same color within an individual image correspond to the same cluster thus indicating a mutual spectral similarity; the average Raman spectra of each cluster of pixels are provided in Figures 7c and 7d and plotted using the color of the corresponding cluster. Similar as for the 100–950 cm^{-1} region, the 20-cycle thin-film sample again exhibits strong spectral differences in terms of intensity, band ratios, spectral shifts, and band broadening in the 900–1550 cm^{-1} region (Figure 7c). Based on the degree of spectral similarity the clusters can again be divided into two groups: group one contains the cluster of color blue, brown,
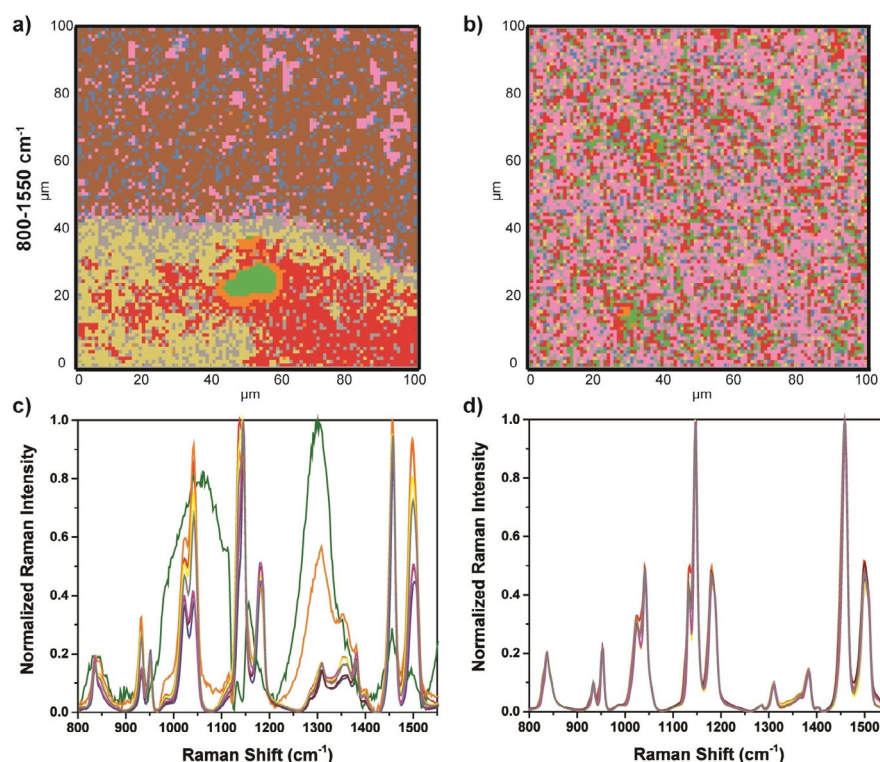
Figure 7. Result of principal component analysis (PCA) and subsequent clustering of the Raman microscopy maps for the 800–1550 cm^{-1} spectral region for both a) the 20-cycle Zn-ZIF-8 thin film and b) the 50-cycle Zn-ZIF-8 thin film. The average Raman spectra belonging to the different clusters obtained from PCA and clustering are displayed in panels c) and d) both for the 20-cycle Zn-ZIF-8 thin film and the 50-cycle Zn-ZIF-8 thin film, respectively. Corresponding colors indicate which spectrum belongs to which cluster.

and magenta, and the second groups consists of the red, yellow, and grey cluster. These differences between the two groups result in the phase boundary observed in Figure 7a, which is located at the same position as in Figure 6a, thus providing a consistent spectroscopic picture of this sample. Specifically, when investigating the Raman spectra displayed in Figure 7c for the main spectral differences in these two distinct groups of clusters in the upper and lower region it becomes clear that these differences arise not only from an intensity-related difference, but also some band broadening and spectral shifts need to be taken into account.

The green and orange clusters indicate the region damaged by the Raman laser exposure as highlighted before. Because the spectral features that correspond to this damage are more dominant in the 900–1550 cm^{-1} region than in the 100–950 cm^{-1} region the segmentation of the hole (green cluster) and its boundary region (orange cluster) is more sensitive in the 900–1550 cm^{-1} region. This is evident from the fact that, when compared to the AFM image, in the map shown in Figure 7a, the shape of the hole is captured much better and, also, a second, smaller hole is detected. Note that this segmentation based on PCA and clustering is exclusively based on spectral features, which highlights the applicability of the approach to correlate spectral and morphological features.

The grey cluster is present mostly in the lower phase and predominantly located across the phase boundary acting as an indicator for an intermediate phase. Furthermore, in Figure 7a in the lower part of the Raman map, there is a sharp transition
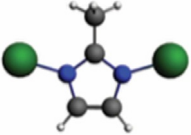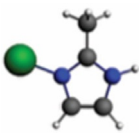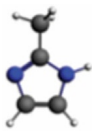
between the yellow and red cluster regions and, by inspecting Figure 7c, this difference can again be attributed to the vibrational bands located at $\approx$1144, $\approx$1180, $\approx$1456 and $\approx$1498 cm^{-1}, i.e., a coupling of ring deformation and C–H bending.

In stark contrast, the Raman map of the 50-cycle thin-film sample, as shown in Figure 7b, displays the well inter-grown nature of this Zn-ZIF-8 thin film, although still chemical heterogeneities can be noted from the distinct Raman spectra observed, for example, for the Raman spectra corresponding to the red, grey and yellow regions. Nevertheless, the intra-sample spectral differences are relatively minor for the 50-cycle thin-film sample (Figure 7d) and the spectra resemble those found in the upper part of the Raman map of the 20-cycle thin-film sample.

Theoretical calculations on SURZIF-8 model systems

From the comparison of AFM and Raman maps for the two Zn-ZIF-8 thin films under investigation it becomes clear that the recorded data describe a unique set of samples, which may provide further insights about the presence of chemical heterogeneities within these thin films and therefore during film growth. By providing a more detailed interpretation of the Raman spectra it might become possible to obtain spectroscopic fingerprints of defects sites present in these framework structures.

In order to do so, we have performed a theoretical investigation to elucidate the origin of the observed spectral features. More specifically, we have performed density functional theory (DFT) calculations for three model systems: the linker (2-methylimidazole) coordinated with two Zn^{2+}-ions, the protonated linker coordinated to one Zn^{2+}, and the isolated protonated linker (with no Zn^{2+}-ions coordinating). These three model structures are visualized in Table 1. For all three models the

Table 1. Labels and structure of the three different model clusters used in DFT calculations to establish spectroscopic fingerprints for investigating and characterizing possible defects in Zn-ZIF-8 thin films (white = H; grey = C; blue = N; and green = Zn).

2 Zn + linker	1 Zn + linker	Linker-only

corresponding Raman spectra have been calculated, and we expect that the 2 Zn + linker model best reflects the structure of the two Zn-ZIF-8 thin films under study. If there is a defect (missing cation), one of the zinc ions will be missing, and subsequently the linker gets protonated (1 Zn + linker model). Finally, the "linker-only" model can be used to check to see whether there are any floating linkers.

The Raman spectra of the 2 Zn + linker, the 1 Zn + linker, and the linker-only models are shown in Figure 8. The most obvious observation is that the Raman intensities of the normal modes up to 1500 cm^{-1} are quite different for the different models. The zinc atoms seem to enhance the Raman intensity in this spectral region; this also means that the Raman intensity above 2800 cm^{-1} is similar for all three models, as the zinc atoms do not take part in the normal modes in that region.

We have therefore in the following focused on the Raman spectra in the region up to 1600 cm^{-1}. In Figure 9 the normal-
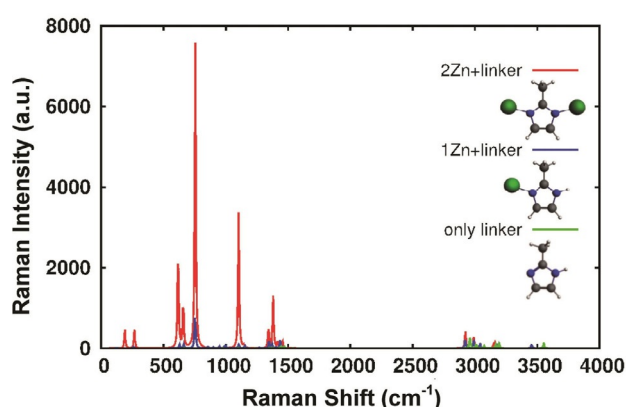

Figure 9. Normalized Raman spectra of the 2 Zn^{2+} + linker, 1 Zn^{2+} + linker, and 'Linker-only" theoretical models as calculated using DFT. The important spectral regions between 230–290 cm^{-1} (region A), 580–680 cm^{-1} (region B), 1050–1180 cm^{-1} (region C), and 1320–1480 cm^{-1} (region D) are zoomed into in the insets, as they contain diagnostic fingerprints for defects sites. The spectra are broadened by a Gaussian profile with half width of 10 cm^{-1} in order to reflect experimental Raman spectra.

ized Raman spectra of the three cluster models are compared. For the 2 Zn + linker and 1 Zn + linker models the normal mode at 754 and 753 cm^{-1}, respectively, were used to normalize the Raman spectra. These normal modes are reported in Supporting Information Table S1.

The first inset of Figure 9 (spectral region A, from 230 to 290 cm^{-1}) shows that the 2 Zn + linker model has one normal mode at 266 cm^{-1}, and the 1 Zn + linker model has two normal modes at 256 and 264 cm^{-1} that overlap to form one peak. The normal mode of 256 cm^{-1} is about 50 to 60% more intense than the peak at 264 cm^{-1} leading to a small but significant shift compared to the 2 Zn + linker model. The linker-only model has one normal mode at 242 cm^{-1} of very low intensity and is not expected to aid much in the characterization of the Zn-ZIF-8 defects in the growing thin films, as observed for our 20 and 50 LBL samples.

It is important to note here that the interpretation of normal modes below 400 cm^{-1} has to be performed with caution, as these normal modes are very sensitive to the environment, and we expect that our theoretical model in this range is less accurate as the force constant of shallow parts of a potential energy surface can significantly shift.

Figure 8. Raman spectra of the 2 Zn + linker, 1 Zn + linker and linker-only models. The spectra are broadened by a Gaussian profile with half width of 10 cm^{-1} in order to reflect experimental Raman spectra. Note that these spectra are not normalized.
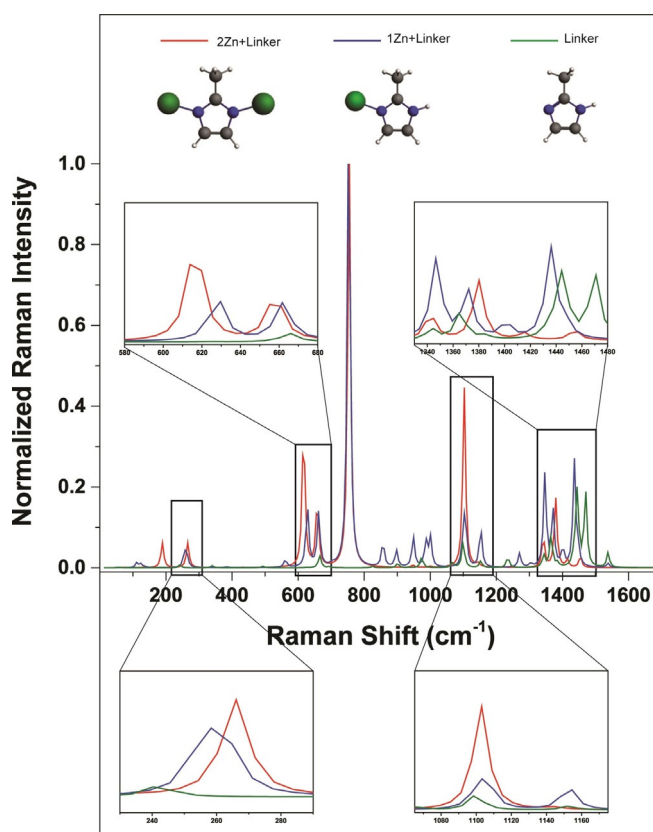
The second inset (spectral region B, from 580–680 cm^{-1}) of Figure 9 shows that there are two normal modes for the 2 Zn + linker and 1 Zn + linker models. The side view and top view of these normal modes can be found in Table S2 in the Supporting Information.

It is worth noting that it is possible to compare the normal modes in this spectral region between the models as they essentially describe the same vibrations. One can ee that the normal mode of 658 cm^{-1} (2 Zn + linker) hardly shifts (blue shift: 4 cm^{-1}) if a metal cation is missing. The reason for this is that this normal mode describes the elongation of the linker molecule perpendicular to the zinc atoms. These atoms, therefore, hardly contribute to the force constant of this vibration. Apparently, the extra N–H bend in the 1 Zn + linker model also does not change the energy of this vibration significantly. The other normal mode in this inset region, however, does shift significantly from 616 cm^{-1} for the 2 Zn + linker model to 628 cm^{-1} for the 1 Zn + linker model (blue shift: 12 cm^{-1}). This normal mode describes the out-of-plane (A'' symmetry) bend of the imidazole linker. We attribute this large blue shift to the loss of symmetry of the normal mode with just one zinc atom. The character of this normal mode becomes more asymmetric and hence shifts towards higher energies. We therefore argue that especially the out-of-plane bending modes of the linker can be used to identify missing metal cations.

The third inset of Figure 9 shows a zoom into the 1050–1180 cm^{-1} region (spectral region C). We can identify three normal modes in this region for all of the models, but the location and the nature of the normal modes are not identical. In Table S3 (see Supporting Information) the top view of these normal modes is visualized. Two out of three normal modes are the same for the different models, but they are shifted in energy and order. The normal mode that describes the C–H symmetric in-plane bending of the imidazole linker does not shift significantly in position (1103 cm^{-1} for 2 Zn + linker, 1106 cm^{-1} for the 1 Zn + linker, and 1100 cm^{-1} for the linker-only model). On the other hand, the in-plane C–H bending mode (1141 cm^{-1} for the 2 Zn + linker model) does shift significantly for the two models in which the imidazole linker is protonated. This is largely caused by the contribution of the N–H bend to the normal mode in these models. Unfortunately, at this time, we cannot explain the large difference of these normal modes between the 1 Zn + linker model (1098 cm^{-1}) and the linker only model (1067 cm^{-1}). Due to the significant shift of these normal modes with the absence of one (or more) zinc atoms, this normal mode seems ideal for identifying defects in the Zn-ZIF-8 thin films. However, as can be seen in the inset in Figure 9 the Raman intensity of this normal mode is not very intense. Moreover, because of the (partial) overlap with the more intense other C–H bending mode, we do not expect large differences in the overall Raman spectra caused by this normal mode. The last normal mode in this region might be able to identify a missing metal cation. The nature of this last normal mode is different for the 2 Zn + linker model compared to the other models. Although the position is only shifted slightly (1145 vs. 1153 cm^{-1}), due to the different

nature of the normal mode, the resulting difference in intensity could be used to identify structural defects.

The fourth inset of Figure 9 shows the 1320–1480 cm^{-1} region (spectral region D), which is rather complex. This region can most definitely be used to characterize defects in growing Zn-ZIF-8 thin films, but the exact elucidation of the shifts in the normal modes is quite difficult. The 2 Zn + linker and the linker-only model systems have both six normal modes in this region, whereas the 1 Zn + linker model system has five normal modes in this region. The top view of these normal modes can be found in Table S4 (Supporting Information). The first thing to note from the normal modes in Table S4 is that all normal modes have a contribution of the methyl group of the imidazole linker. Moreover, the coupling between the contribution of the methyl group and the contribution of the other C–H bends of the linker is quite complex, and therefore, a direct comparison between the normal modes of the different model systems is not (always) possible. If there is a missing linker we expect on the basis of our calculated Raman spectra that there is a shift in intensity of the normal mode of 1346 cm^{-1} (for the 1 Zn + linker). This normal mode becomes more intense than the normal mode of 1371 cm^{-1}, whereas for the 2 Zn + linker system the normal mode at 1380 cm^{-1} remains more intense than the combination of the normal modes of 1342 cm^{-1} and 1353 cm^{-1}. The normal mode at 1436 cm^{-1} is also very intense for the 1 Zn + linker model system, whereas the 2 Zn + linker model system has no intense normal modes between 1400 and 1480 cm^{-1}. Finally, the linker-only model system has two intense normal modes at 1445 and 1470 cm^{-1}. Especially the peak arising at 1470 cm^{-1} can be used to determine whether there are floating linkers in the Zn-ZIF-8 thin film.

Spectroscopic fingerprinting of chemical heterogeneities in SURZIF-8 thin films

Having now more in-depth insights into the vibrational fingerprints of the different Zn^{2+} and 2-methylimidazole coordination environment combinations we are in the position to turn back to the experimentally measured Raman spectra, as reported in Figures 6 c,6 d and 7 c,7 d, for the spectral regions 100–950 cm^{-1} and 800–1550 cm^{-1} and the 20-cycle and 50-cycle thin-film samples, respectively. The detailed investigation and comparison of the first spectral region of 250–320 cm^{-1} for the 20-cycle and 50-cycle thin-film samples are provided in Figure 10 a and 10 c, respectively, and allows now to use the insights gathered from the discussions of spectral region A of Figure 9. The vibrational band located at ≈284 cm^{-1} was assigned as ring deformation in accordance with the DFT calculations. Individual inspection of the spectra of each cluster in the 20-cycle thin-film sample indicates that the spectra of yellow and magenta clusters (and the green cluster, which corresponds to the hole region) undergo a larger red shift and band broadening than the other clusters. This group (yellow, magenta) forms the lower part of the Raman map, whereas the other clusters gray, brown, and orange form the upper part of the phase boundary and show larger spectral heterogeneity. Spectroscopically, the red and blue clusters represent an
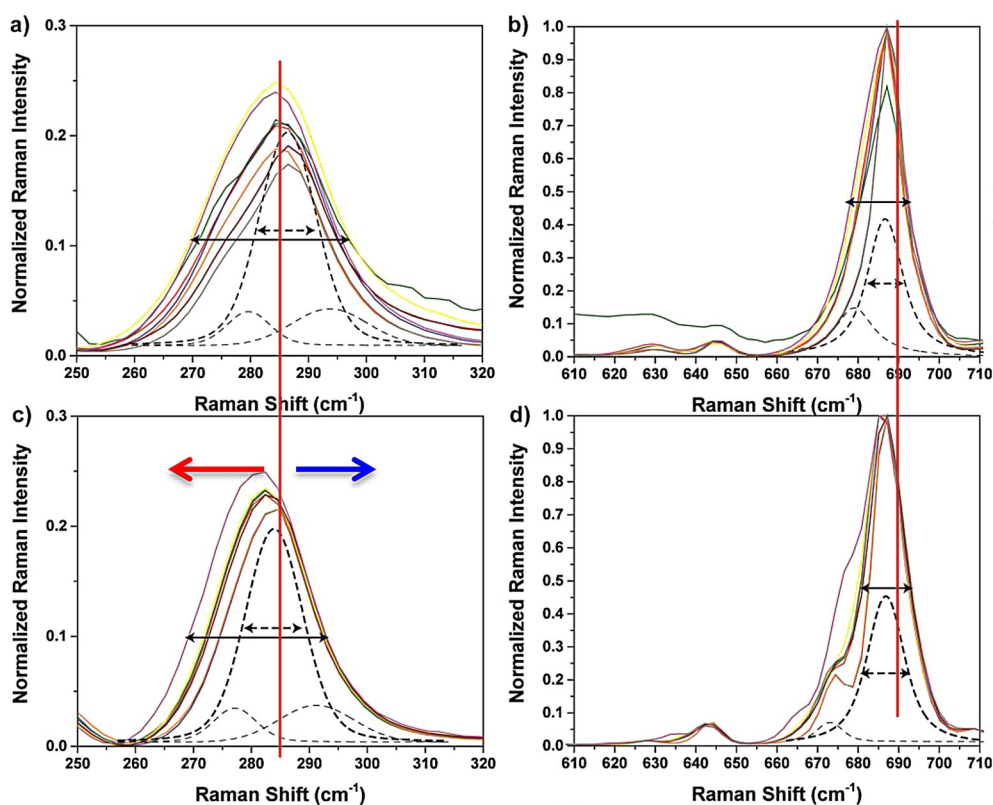
Figure 10. Comparison of the zoomed-in Raman bands (Figure 6c & 6d) belonging to the clusters resulting from PCA and clustering analysis for a),b) the 20-cycle and c),d) 50-cycle thin film located at ≈ 284 and ≈ 686 cm^{-1}, respectively. The Raman spectra have been fitted with individual bands to guide the eye when discussing the band broadenings and spectral shifts in the main text.

intermediate phase between those two groups and have very similar average spectra. The blue cluster is found in both the upper and lower regions and is also populated around the phase boundary highlighting its intermediate nature also spatially, that is, through its distribution in the Raman map. When comparing this band region of the clusters with the correlated AFM-Raman data (Figures 4 and 5c–g), it is clear that the highest regions of the thin film display differences in these spectral bands when compared to the other areas of the sample. The differences are indicated by black arrows in Figure 5c–g. However, the Raman spectra of the highest regions are most similar to the spectra of the grey and brown clusters, that is, the scattered regions found in the upper half of the Raman map.

Figure 10c shows the presence of a red shift and a band broadening in this region also for the 50-cycle sample; however, these variations are minor and result in a more homogeneous inter-grown nature of the sample as shown in Figure 6b. A larger band broadening and spectral shift together with the appearance of a weak shoulder is especially apparent in the spectra of the 20-cycle sample when compared to its 50-cycle analogue of the ZIF-8 thin film. The spectral red shift was found in the order of ≈ 5 cm^{-1} and the band broadening was calculated in terms of FWHM and was found to be between ≈ 11 to 17 cm^{-1} for the 20-cycle sample. For the 50-cycle sample the red shift was calculated to be only ≈ 2 cm^{-1} and the FWHM values vary in the order of ≈ 6–10 cm^{-1}, which are also minor. These spectral observations are all in line with a

more ordered Zn-ZIF-8 for the 50-cycle sample, as well as the presence of less defect sites in comparison with the 20-cycle sample.

A comparison of this spectral fitting with the spectral data obtained through computational simulation indicates that the vibrational modes arising from a missing linker together with one Zn^{2+} undergo a huge band broadening along with the appearance of a shoulder as well as a spectral red shift when compared to the vibrational mode containing one linker and two Zn^{2+} ions. These results suggest that the clusters forming the lower region of the Raman map shown in Figure 6a have defects arising from the absence of one Zn^{2+} ion resulting in a loss of symmetry of the normal mode and hence a band broadening. On the other hand, the clusters forming the upper region of the phase boundary in Figure 6a show a relatively lower band broadening compared to the lower part of the Raman map as mentioned previously and have similarities with the clusters forming the 50-cycle thin-film material indicating a higher degree of symmetry, that is, the vibrational mode is arising from the presence of two zinc cations bonded to a linker.

The detailed investigation and comparison of the spectral region of 610–710 cm^{-1} for the 20-cycle and 50-cycle samples are provided in Figure 10b and 10d, respectively, where we can now apply the insights obtained from the previous discussion of spectral region B. The vibrational band located at ≈ 686 cm^{-1} was assigned to C–H bending/ring deformation in

accordance with the DFT calculations as provided in Table S2 (see Supporting Information). The individual analysis of the spectra of the clusters regarding the band located at ≈686 cm^{-1} for the 20-cycle sample shows similarities with the band located at ≈284 cm^{-1} in terms of the distribution of the clusters throughout the upper and lower parts of the phase boundary observed in Figure 6a. To illustrate, the spectra of the magenta and yellow clusters (the green cluster indicates the hole in the sample) are exposed to the highest red shift and band broadening and these regions form the lower part of the observed phase boundary. On the other hand, in the case of 50-cycle sample, the most striking observation is the appearance of a shoulder at a lower wavenumber with a maximum at ≈675 cm^{-1} for the band located at ≈686 cm^{-1}. For this sample the spectra of the magenta and orange clusters differ most between each other, but also with respect to the spectra of the other clusters. The spectrum of the magenta cluster has a less defined shoulder with higher intensity, whereas the spectra of the orange and blue clusters undergo the smallest band broadening of all spectra and show a very well-defined shoulder.

The comparison of the spectra of individual clusters of the 20-cycle and 50-cycle ZnZIF-8 thin-film materials reveals a similar order of band broadening as well as a spectral red shift as for spectral region A. The calculated FWHM values regarding the band located at ≈686 cm^{-1} vary in the range of ≈6–10 cm^{-1} for both samples and the spectral red shift was found

in the order of ≈2 and ≈1 cm^{-1} for the 20-cycle and 50-cycle samples, respectively. The band maxima of the ≈686 cm^{-1} band were found to be identical for both samples and all clusters. The comparison of the experimental results with the spectra obtained through DFT calculations indicates that the vibrational mode arising from a missing zinc cation lacks the presence of a shoulder and the band maximum is located at higher wavenumber than the vibrational mode of the two zinc cations and linker system. These results suggest that the presence of a shoulder at ≈675 cm^{-1} in the spectra of the clusters of the 50-cycle sample can be explained by the presence of two zinc cations and linker, whereas the absence of this shoulder in the spectra of the 20-cycle sample implies that there is at least a fraction of the sample that is missing a zinc cation, indicating a loss of symmetry in the overall thin-film structure.

The detailed investigation and comparison of the spectral region of 1075–1225 cm^{-1} (spectral region C) for the 20-cycle and 50-cycle thin-film samples are provided in Figure 11a and 11c, respectively. The vibrational bands located at ≈1144 and ≈1180 cm^{-1} were assigned as C–H bending and ring deformation in accordance with the DFT calculations, as provided in Table S3. Detailed investigation of the individual spectra of each cluster for the 20-cycle sample shows that the Raman band located at ≈1144 cm^{-1} undergoes a change in terms of band broadening along with the appearance of a new shoulder-like band located at ≈1135 cm^{-1} (Figure 11a). The spectra
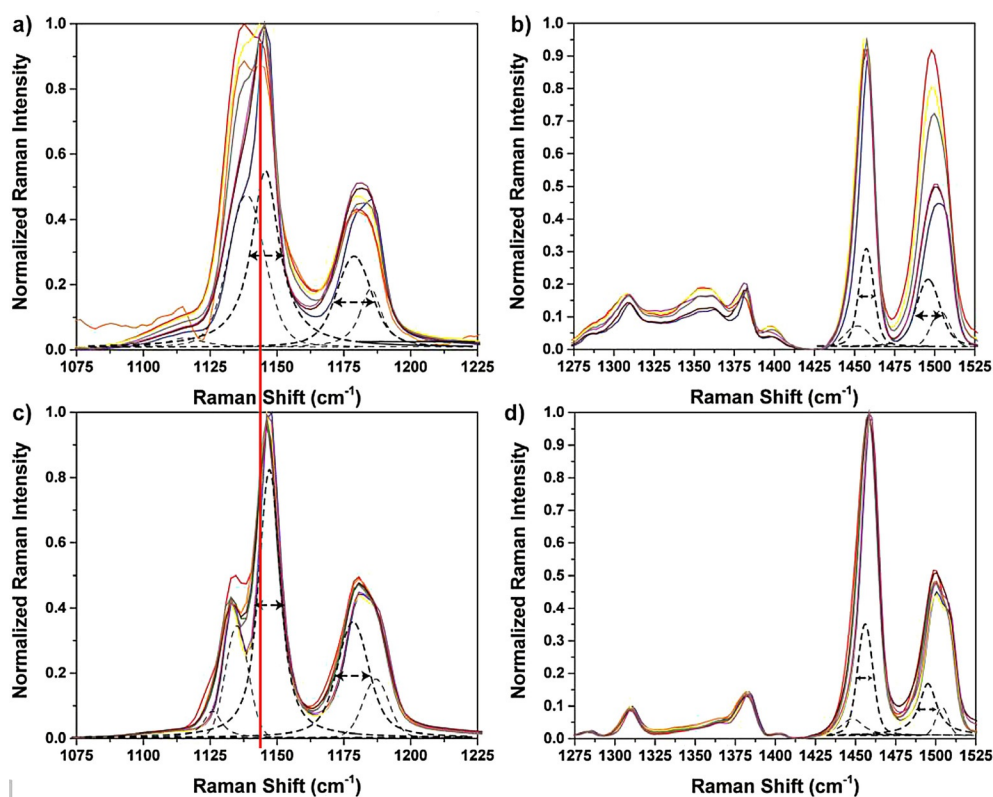

Figure 11. Comparison of the zoomed-in Raman bands (Figure 7c & 7d) belonging to the clusters resulting from PCA and clustering analysis for a),b) the 20-cycle and c),d) the 50-cycle thin film located at ≈1144, ≈1180, ≈1456 and ≈1498 cm^{-1}. The Raman spectra have been fitted with individual bands to guide the eye when discussing the band broadenings and spectral shifts in the main text.

of the red, yellow, and grey clusters have the largest band broadening and the appearance of a new Raman band is clearly visible (similar spectral features were detected for the orange cluster, which is, however, indicating the interface between thin film and hole and therefore needs to be interpreted with caution). These clusters differ most from the other clusters and form the lower part of the Raman map in Figure 7a, that is, below the phase boundary where the grey cluster acts as an intermediate, both spectroscopically and when inspecting its spatial distribution in the Raman map. The analysis of the Raman band located at ≈ 1144 cm^{-1} was also performed for the 50-cycle sample. The appearance of the new band becomes clearly visible at ≈ 1135 cm^{-1}, but with relatively lower intensities. The spectra of red, magenta, blue, and yellow are different from the spectra of the other clusters (green, brown, orange, grey). The shoulder in the spectrum belonging to the red cluster has the highest Raman band intensity, whereas the broadening of the well-defined shoulder appearing in the spectra of the magenta, blue, and yellow cluster as well as the broadening of the main band are much lower than the broadening of those bands in all other spectra, which causes the two bands to be much better separated in these clusters (yellow, blue, magenta).

The comparison of the 20-cycle and 50-cycle sample concerning the aforementioned band (and band splitting) indicates that the band broadening for the ≈ 1144 cm^{-1} vibrational band is found to be almost two times larger for the 20-cycle sample (≈ 8–21.5 cm^{-1}) than for the 50-cycle sample (≈ 8.6–10 cm^{-1}). In order to explain these observed differences, the DFT calculations can again provide further insights. The vibrational mode arising from the missing zinc cation possessing a low degree of symmetry exhibits a shoulder at higher intensities in contrast to the vibrational mode simulated in the case of two zinc cations and a linker. The appearance of a shoulder at higher intensities is the observation that we made in the case of the 20-cycle sample in particular in the spectra of the clusters (red, yellow, orange and grey) forming the lower part of the Raman map (Figure 7a). Furthermore, in the theoretical spectra, this band is broader (higher FWHM) and this is also the case for the 20-cycle sample. This shoulder is also visible in the 50-cycle sample, but the intensity of the shoulder is drastically reduced, indicating a relatively higher degree of symmetry. On the other hand, the Raman band maximum regarding the band located at ≈ 1146 cm^{-1} in the theoretical Raman spectra is located at higher wavenumber in the case of a missing zinc cation.

Furthermore, the second Raman band located at ≈ 1180 cm^{-1}, still in spectral region C of the Raman spectra, was also investigated in detail. Figure 11a and 11c illustrate the individual spectra of each cluster for the aforementioned band for the 20-cycle and 50-cycle thin films, respectively. The comparison of the spectra of individual clusters in the 20-cycle sample shows differences in terms of band broadening, spectral shift and the appearance of a shoulder, particularly visible in the blue cluster. The spectra of the yellow, red, orange and grey clusters have relatively lower ≈ 1180 cm^{-1} band intensities when compared with the other clusters. In contrast, for the 50-cycle thin film this band is very similar for all clusters, and overall does not provide much discriminative power to identify defects sites in the different regions of interest and between the two samples.

The last and fourth spectral Raman region of interest covering the region between 1275 and 1525 cm^{-1} was also investigated in detail, as shown in Figure 11b and 11d for the 20-cycle and 50-cycle thin films of ZnZIF-8, respectively. This region can now be discussed together with the theoretical insights provided by DFT and as discussed for spectral region D (Figure 9). The vibrational bands located at ≈ 1458 and ≈ 1498 cm^{-1} are assigned to C–H bending and ring deformation (Table S4). In the 20-cycle sample, the Raman bands located at ≈ 1458 cm^{-1} and ≈ 1498 cm^{-1} exhibit differences throughout the spectra of clusters in terms of band broadening and spectral shifts. The bands that are broadened most belong to the spectra of the red, yellow, and grey cluster; and are more dominant for the ≈ 1498 cm^{-1} than for the ≈ 1458 cm^{-1} band. This is again in line with the observations made when inspecting the other bands, as these clusters form the lower part of the Raman map provided in Figure 7c. On the other hand, band broadening is also observed in the case of the 50-cycle sample for the ≈ 1458 cm^{-1} and ≈ 1498 cm^{-1} bands. However, the resulting Raman map of all clusters, as illustrated in Figure 7b, shows the inter-grown nature of the film under study. The comparison of the band broadening and spectral shift regarding the ≈ 1458 cm^{-1} vibrational band between 20-cycle and 50-cycle sample demonstrates that the average calculated FWHM was found to be higher for the 50-cycle sample (≈ 12–14 cm^{-1}) sample than the 20-cycle sample (≈ 9–12 cm^{-1}) sample, while the Raman band maxima are at very similar positions for both ZnZIF-8 thin films. Furthermore, the average spectral shift was found to be in the order of ≈ 2 cm^{-1} for both samples, which is very small, and therefore at the very limit of experimental accuracy.

The second vibrational band of interest in the spectral region of 1275–1525 cm^{-1} is the band located at ≈ 1498 cm^{-1} and a detailed analysis was also performed for this band. In the Raman spectra of the 20-cycle sample, the comparison of the individual spectra of each cluster shows big differences in terms of band broadening, spectral shift, and intensity differences. The most striking observation is the decrease in the band intensity as going from the red to the yellow and grey to the remaining clusters. These clusters (red, yellow, grey), which possess a higher band intensity of this band are again responsible for the appearance of the observed phase-boundary and form the lower part of the Raman map shown in Figure 7a. Inspecting the same band for the 50-cycle sample reveals also differences in terms of band broadening and spectral shifts, but clearly this band is much less intense as in the case of the 20-cycle sample. An appearance of a shoulder at ≈ 1508 cm^{-1} is also observed. The calculated FWHM of the band located at ≈ 1498 cm^{-1} varies in the range of ≈ 17–21 cm^{-1} and ≈ 14–19 cm^{-1} and the calculated spectral shift is found to be in the order of ≈ 3 to ≈ 2.5 cm^{-1} for the 20-cycle and 50-cycle samples, respectively. The Raman band maxima are also located at very similar positions for both samples.

Conclusion

Two distinct thin films of Zn-ZIF-8, obtained after 20 and 50 layer-by-layer (LBL) cycles, have been prepared and subsequently characterized by Raman micro-spectroscopy as well as atomic force microscopy (AFM). A region of 100×100 μm^2 was imaged and a detailed spectral and topographic mapping was performed in order to search for chemical heterogeneities in these two thin-film materials. Principal component analysis (PCA) and clustering of the acquired Raman data demonstrated the existence of a clear phase boundary in the 20-cycle Zn-ZIF-8 thin film, whereas the 50-cycle Zn-ZIF-8 thin film is chemically much more homogeneous in nature, although still rich in chemical heterogeneities.

The spectral differences observed between the different phases present in the samples were studied through a detailed analysis of the Raman spectroscopy data. In order to assist the search for vibrational fingerprints of defects sites we performed density functional theory (DFT) calculations on three model systems, namely the linker (i.e., 2-methylimidazole) co-ordinated with two Zn^{2+}-ions, a protonated linker coordinated to one Zn^{2+}, and an isolated protonated linker (with no Zn^{2+}-ions coordinating to the linker). This theoretical approach enabled the calculation of the molecular vibrations of the fingerprint spectral features of Zn-ZIF-8 thin films, undergoing intensity changes and/or band splitting/shifts.

Based on this detailed comparison of both the experimental and theoretical Raman spectra in four distinct spectral regions (A–D) for the two Zn-ZIF-8 thin films under study it was found that:

- Spectral region A (230–290 cm^{-1}) provides information on the overall structural quality of the thin film via the 284 cm^{-1} Raman band. When this band becomes broad and red-shifted the region becomes more defect-rich.

- Spectral region B (580–680 cm^{-1}) provides information on the overall structural quality of the thin film via the relative intensity ratio of the 675 and 686 cm^{-1} Raman bands. A more intense 675 cm^{-1} Raman band is indicative of a defect-poor structure.

- Spectral region C (1065–1175 cm^{-1}) provides information on the overall structural quality of the thin film via the 1180 cm^{-1} band, as this band is characteristic for the presence of a linker with only one Zn^{2+} ion. As this band is also present in a well-formed thin film it indicates that even for such material there are some Zn^{2+} ions missing in the ZIF-8 structure.

- Spectral region C (1065–1175 cm^{-1}) provides additional information on the overall structural quality of the thin film via the relative intensity ratio of the 1135 and 1144 cm^{-1} Raman bands. A more intense 1135 cm^{-1} Raman band is indicative of a defect-rich structure.

- Spectral region D (1320–1480 cm^{-1}) provides direct information on the presence of free linkers via the presence of the 1498 cm^{-1} Raman band. Clearly, sample regions, which are defect-rich have a high intensity of this Raman band, although our data also suggest that even for more defect-

free regions there are still some free linkers present. The relative intensity ratio of the 1458 and 1498 cm^{-1} Raman bands turns out to be a quality indicator for the structural integrity of the Zn-ZIF-8 thin film. A more intense 1458 cm^{-1} Raman band is indicative of a defect-poor structure.

Summarizing, this work provides Raman spectroscopy fingerprints for evaluating the overall quality and presence of different defect sites within SURZIF-8 thin films, although it should be clear that the procedure developed is much more generally applicable to other ZIF and MOF materials.

Experimental Section

Layer-by-layer synthesis of Zn-ZIF-8 thin films: The synthesis of Zn-ZIF-8 thin films was carried out through a layer-by-layer (LBL) method, which was adapted from a study by Eddaoudi et al.[19] The synthesis was performed through an automated peristaltic pump system in a home-built glass set up. 10 mM of a 11-mercapto-1-undecanol (MUD) (Sigma–Aldrich, 97%) ethanolic solution (Acros, extra dry) was used for the modification of gold-coated silicon wafers. 10×10 mm of 60 nm Au coated Si wafers with Ge adhesion layer were purchased from Amolf (FOM institute, the Netherlands). Au-coated substrates were first cleaned in a UV-ozone cleaner for 15 min and then placed into vials containing 2 mL of 10 mM MUD ethanolic solution for 4 h. After 4 h of self-assembly, Au-coated substrates were dried under gentle N$_2$ stream and were placed into a glass set up. 100 mM and 50 mM of Zn(NO$_3$)$_2$·6H$_2$O (Sigma–Aldrich, 99%) and 2-methylimidazole (Sigma–Aldrich, 99%) methanolic (Acros, extra dry) solutions were prepared, respectively. 2 and 3 min deposition times were applied for 1.5 mL of Zn^{2+} and 2-methylimidazolate methanolic solutions, respectively at room temperature. The Au-coated substrates were rinsed with fresh methanol between each step, in order to remove unreacted species. This deposition process composed of four subsequent steps corresponds to 'one cycle' of deposition. In this work, two SURZIF-8 samples have been prepared with 20 and 50 LBL cycles.

Characterization of bulk Zn-ZIF-8 and Zn-SURZIF-8 thin film: Raman spectroscopy measurements were performed with a Renishaw InVia micro-spectrometer making use of a 785 nm laser and the spectra were recorded in the region of 100–3200 cm^{-1}. For all measurements a 785 nm laser was used with 600 lines per millimeter grating. The spectra during the Raman measurements were recorded in a region of 100×100 μm^2 with the grating at a static position with the spectral centers at 520 and 1180 cm^{-1}. Atom force microscopy (AFM) measurements of 100×100 μm^2 scans were executed for the samples with high resolution (1024×1024 pt^2) in order to obtain topographical information. The AFM scans were conducted on a NT-MDT NTEGRA Spectra upright AFM unit and Olympus AC 160TS tips were used for all AFM measurements.

Segmentation of the AFM data: First, AFM images were thresholded removing the lowest X% of the heights as the image background. The threshold X was set to 52% for the 20 and to 40% for the 50 cycles samples, respectively, in order to account for the hole in the 20 cycles data set. The region of the hole contained the lowest 12% of recorded heights in the 20 cycles sample, therefore causing an offset of 118.7 nm for the height recorded everywhere else in the image. Because the 50 cycles sample did not contain such a hole these 12% were added to the background threshold for the 20 cycles sample in order to correctly identify grains on top

of the grown film for a comparison of both samples. In this way the background ("height zero") was defined as the lowest measured elevation of the film for both samples and not the height in the hole for the 20 cycles sample. After thresholding the images were converted into binary images using adaptive thresholding applying Bradley's method,[39] that is, by calculating a threshold for each pixel using the local mean gray scale intensity around the neighborhood of the pixel. Next, all isolated regions were identified in the binary image and regions that consisted of less than 5 pixels were removed (noise removal). Then each region was analyzed computing its area, its equivalent diameter (based on a circle of equal area as the region), its eccentricity, major and minor axis length, and its orientation. Region eccentricity, major and minor axis length, and orientation are based on an ellipse that has the same second-moments as the region. The eccentricity is a value between 0 and 1 and indicates the ratio of the distance between the foci of the ellipse and its major axis length (an eccentric of 0 indicates a circle). The region orientation specifies the angle between the x-axis and the major axis of the ellipse. All processing was implemented using in-house developed Matlab™ code.

Data processing and analysis: Principal component analysis (PCA)[40] was performed for the analysis of the micro-spectroscopy data after background subtraction and normalization. A spectral map consisted of 101×101 pixels, that is, $M = 10\,201$ spectra with each spectrum consisting of $W = 393$ measured wavenumbers at every pixel. PCA was used to reduce the dimensions of this dataset from a dataset of size $M \times W$ to a dataset of size $M \times N$, in which N was significantly smaller than W, effectively reducing the dimensionality of the data set without losing relevant information by preserving most of the variance in the data.[41,42] PCA produces principal components (PCs) that are linear combinations of the W independent original variables (here wavenumbers). The PCs further form an orthonormal basis set that is aligned to best express the data with respect to its variance. Every PC covers a fraction of the data's variance, which in turn is used to assess the importance of each PC to describe the data set ("variance explained" of each PC). The PCs were determined by singular value decomposition (SVD) of the M x W matrix resulting in a new matrix $M \times PC_{1-W}$, where the PCs (columns) are eigenimages, while the rows represent eigenspectra. In this representation there are still W PCs, but this number can now be reduced to N PCs, by keeping only the PCs that describe most of the variance (information) in the data. In this study, the first four PCs ($N = 4$) were retained based on an inspection of the cumulative variance explained (CVE) by all PCs. In this reduced data set every pixel M is now characterized by four parameters (the "scores" of the 4 PCs) that are a linear combination of the original W parameters (wavenumbers). By plotting the M pixels in this 4-dimensional space defined by the orthonormal basis set formed by the PCs (score plot), one can learn about the similarity of two spectra (pixels) by looking at their (Euclidean) distance within this plot. The closer two points are in this space the more similar are their spectra and thus their chemical identity. Here it is important to point out that this distance is purely based on spectral similarity of the data points (pixels) and completely independent of any spatial proximity, that is, their location in the sample. We therefore used k-means clustering[43,44] and a Euclidean distance metric to pool data points in 4-dimensional PC space, that is, group pixels with most similar spectral fingerprints. k-Means clustering requires an a priori definition of the number of clusters; in this work we therefore followed to approach to first intentionally over-cluster the data set using eight clusters (twice the number of principal components). Then in a second, refining step we performed a density-based clustering applying a Gaussian Mixture Model (GMM)

and using the result of the k-means clustering as an initial guess. Because the result of the GMM clustering returns a class membership value for each data point the average Raman spectrum of each cluster was obtained via the weighted average of all spectra of a cluster, that is, considering the degree to which each pixel belongs to every cluster.

Theoretical calculations: Density functional theory (DFT) calculations have been performed to obtain the vibrational frequencies of model systems of SURZIF-8 systems and their building blocks. Geometry optimization of these systems and the related constituents were performed with the ADF program package[45] using the PBE functional[46] and a TZP basis set.[47] For the frequency analysis of the FT-IR spectra the analytical gradients were used.[48–50] The Raman spectroscopy theoretical calculations[51,52] used a laser frequency of 1.58 eV corresponding to the experimental laser used (785 nm). In order to compare better with experimental spectra, the theoretically calculated frequencies of the Raman spectra were broadened by a Gaussian with a half width of 10 cm^{-1}.

Acknowledgements

Conflict of interest

The authors declare no conflict of interest.

[1] P. St. Petkov, G. N. Vayssilov, J. Liu, O. Shekhah, Y. Wang, C. Wöll, T. Heine, *ChemPhysChem* **2012**, *13*, 2025 – 2029.
[2] H. B. Tanh Jeazet, C. Staudt, C. Janiak, *Dalton Trans.* **2012**, *41*, 14003 – 14027.
[3] G. Férey, *Chem. Soc. Rev.* **2008**, *37*, 191 – 214.
[4] Z. Öztürk, J. P. Hofmann, M. Lutz, M. Mazaj, N. Z. Logar, B. M. Weckhuysen, *Eur. J. Inorg. Chem.* **2015**, 1625 – 1630.
[5] S. Horike, M. Dincă, K. Tamaki, J. R. Long, *J. Am. Chem. Soc.* **2008**, *130*, 5854 – 5855.
[6] L. T. L. Nguyen, K. K. A. Le, H. X. Truong, N. T. S. Phan, *Catal. Sci. Technol.* **2012**, *2*, 521 – 528.
[7] M. Ranocchiari, J. A. van Bokhoven, *Phys. Chem. Chem. Phys.* **2011**, *13*, 6388 – 6396.
[8] S. Keskin, K. Seda, *Ind. Eng. Chem. Res.* **2011**, *50*, 1799 – 1812.
[9] K. M. L. Taylor-Pashow, J. Della Rocca, S. Xie, S. Tran, W. Lin, *J. Am. Chem. Soc.* **2009**, *131*, 14261 – 14263.
[10] L. Zhang, Y. Jian, J. Wang, C. He, X. Li, T. Liu, C. Duan, *Dalton Trans.* **2012**, *41*, 10153 – 10155.
[11] L. He, Y. Liu, J. Liu, Y. Xiong, J. Zheng, Y. Liu, Z. Tang, *Angew. Chem. Int. Ed.* **2013**, *52*, 3741 – 3745; *Angew. Chem.* **2013**, *125*, 3829 – 3833.
[12] J. A. Botas, G. Calleja, M. Sánchez-Sánchez, M. G. Orcajo, *Langmuir* **2010**, *26*, 5300 – 5303.
[13] G. Kumari, K. Jayaramulu, T. K. Maji, C. Narayana, *J. Phys. Chem. A* **2013**, *117*, 11006 – 11012.

[14] S. Couck, E. Gobechiya, P. Serra-Crespo, A. Martinez Joaristi, E. Stavitski, J. Gascon, F. Kapteijn, G. V. Baron, J. F. M. Denayer, *ChemSusChem* **2012**, *5*, 740 – 750.

[15] J. Yao, H. Wang, *Chem. Soc. Rev.* **2014**, *43*, 4470 – 4493.

[16] K. S. Park, Z. Ni, A. P. Cote, J. Y. Choi, R. Huang, F. J. Uribe-Romo, H. K. Chae, M. O'Keeffe, O. M. Yaghi, *Proc. Natl. Acad. Sci. USA* **2006**, *103*, 10186 – 10191.

[17] A. Phan, C. J. Doonan, F. J. Uribe-Romo, C. B. Knobler, M. O'Keeffe, O. M. Yaghi, *Acc. Chem. Res.* **2010**, *43*, 58 – 67.

[18] E. L. Bustamante, J. L. Fernández, J. M. Zamaro, *J. Colloid Interface Sci.* **2014**, *424*, 37 – 43.

[19] O. Shekhah, R. Swaidan, Y. Belmabkhout, M. du Plessis, T. Jacobs, L. J. Barbour, I. Pinnau, M. Eddaoudi, *Chem. Commun.* **2014**, *50*, 2089.

[20] Y. Hu, H. Kazemian, S. Rohani, Y. Huang, Y. Song, *Chem. Commun.* **2011**, *47*, 12694 – 12696.

[21] A. Huang, Q. Liu, N. Wang, J. Caro, *J. Mater. Chem. A* **2014**, *2*, 8246.

[22] J. Cookney, W. Ogieglo, P. Hrabanek, I. Vankelecom, V. Fila, N. Benes, *Chem. Commun.* **2014**, *50*, 11698 – 11700.

[23] S. R. Venna, J. B. Jasinski, M. A. Carreon, *J. Am. Chem. Soc.* **2010**, *132*, 18030 – 18033.

[24] P. Y. Moh, P. Cubillas, M. W. Anderson, M. P. Attfield, *J. Am. Chem. Soc.* **2011**, *133*, 13304 – 13307.

[25] O. Shekhah, J. Liu, R. A. Fischer, C. Wöll, *Chem. Soc. Rev.* **2011**, *40*, 1081 – 1106.

[26] A. Bétard, R. A. Fischer, *Chem. Rev.* **2012**, *112*, 1055 – 1083.

[27] D. Zacher, O. Shekhah, C. Wöll, R. A. Fischer, *Chem. Soc. Rev.* **2009**, *38*, 1418 – 1429.

[28] H. Guo, Y. Zhu, S. Qiu, J. A. Lercher, H. Zhang, *Adv. Mater.* **2010**, *22*, 4190 – 4192.

[29] E. Biemmi, A. Darga, N. Stock, T. Bein, *Microporous Mesoporous Mater.* **2008**, *114*, 380 – 386.

[30] R. Ameloot, L. Stappers, J. Fransaer, L. Alaerts, B. F. Sels, D. E. De Vos, *Chem. Mater.* **2009**, *21*, 2580 – 2582.

[31] S. Aguado, J. Canivet, D. Farrusseng, *Chem. Commun.* **2010**, *46*, 7999 – 8001.

[32] E. V. Ramos-Fernandez, M. Garcia-Domingos, J. Juan-Alcañiz, J. Gascon, F. Kapteijn, *Appl. Catal. A* **2011**, *391*, 261 – 267.

[33] Y. Yoo, Z. Lai, H.-K. Jeong, *Microporous Mesoporous Mater.* **2009**, *123*, 100 – 106.

[34] V. V. Guerrero, Y. Yoo, M. C. McCarthy, H.-K. Jeong, *J. Mater. Chem.* **2010**, *20*, 3938 – 3943.

[35] A. Bétard, H. Bux, S. Henke, D. Zacher, J. Caro, R. A. Fischer, *Microporous Mesoporous Mater.* **2012**, *150*, 76 – 82.

[36] D. Zacher, K. Yusenko, A. Bétard, O. Shekhah, T. de los Arcos, M. Krasnopolski, J. Winter, A. Terfort, C. Wöll, R. A. Fischer, *Chem. Eur. J.* **2011**, *17*, 1448 – 1455.

[37] D.-Y. Kim, B. N. Joshi, J.-G. Lee, J.-H. Lee, J. S. Lee, Y. K. Hwang, J.-S. Chang, S. Al-Deyab, J.-C. Tan, S. S. Yoon, *Chem. Eng. J.* **2016**, *295*, 49 – 56.

[38] S. Tanaka, K. Fujita, Y. Miyake, M. Miyamoto, Y. Hasegawa, T. Makino, S. Van der Perre, T. Van Assche, G. V. Baron, J. F. M. Denayer, *J. Phys. Chem. C* **2015**, *119*, 28430 – 28439.

[39] D. Bradley, G. Roth, *J. Graph. Tools* **2007**, *12*, 13 – 21.

[40] R. Bro, A. K. Smilde, *Anal. Methods* **2014**, *6*, 2812 – 2831.

[41] J. E. Jackson, *A User's Guide to Principal Components*, Wiley-Interscience, Hoboken, NJ, **2003**.

[42] I. T. Joliffe, *Principal Component Analysis*, Springer, New York, **2002**.

[43] J. B. MacQueen, in *5th Berkeley Symposium on Mathematical Statistics and Probability*, University Of California Press, Berkeley, CA, **1967**.

[44] R. A. Johnson, D. W. Wichern, *Applied Multivariate Statistical Analysis*, Pearson, Upper Saddle River, NJ, **2002**.

[45] G. te Velde, F. M. Bickelhaupt, E. J. Baerends, C. Fonseca Guerra, S. J. a. van Gisbergen, J. G. Snijders, T. Ziegler, *J. Comput. Chem.* **2001**, *22*, 931 – 967.

[46] B. K. Perdew, J. P. M. Ernzerhof, *Phys. Rev. Lett.* **1996**, *77*, 3865 – 3868.

[47] E. Van Lenthe, E. J. Baerends, *J. Comput. Chem.* **2003**, *24*, 1142 – 1156.

[48] A. Bérces, R. M. Dickson, L. Fan, H. Jacobsen, D. Swerhone, T. Ziegler, *Comput. Phys. Commun.* **1997**, *100*, 247 – 262.

[49] H. Jacobsen, A. Bérces, D. P. Swerhone, T. Ziegler, *Comput. Phys. Commun.* **1997**, *100*, 263 – 276.

[50] S. K. Wolff, *Int. J. Quantum Chem.* **2005**, *104*, 645 – 659.

[51] S. J. A. van Gisbergen, J. G. Snijders, E. J. Baerends, *Chem. Phys. Lett.* **1996**, *259*, 599 – 604.

[52] S. J. A. van Gisbergen, J. G. Snijders, E. J. Baerends, *Comput. Phys. Commun.* **1999**, *118*, 119 – 138.